Journal of Structural Biology 170 (2010) 41–49

Contents lists available at ScienceDirect

Journal of Structural Biology

journal homepage: www.elsevier.com/locate/yjsbi

Structure, composition and mechanical relations to function in sea urchin spine

C. Moureaux [a,*], A. Pérez-Huerta [b], P. Compère [c], W. Zhu [d], T. Leloup [e], M. Cusack [f], P. Dubois [a]

[a] Laboratoire de Biologie Marine, Université Libre de Bruxelles, Brussels, Belgium
[b] Department of Geological Sciences, University of Alabama, Tuscaloosa, USA
[c] Laboratoire de Biologie Générale et Morphologie Ultrastructurale, Université de Liège, Liège, Belgium
[d] School of Engineering and Science, University of the West of Scotland, Paisley, Scotland, UK
[e] Laboratory of Image Synthesis and Analysis, Université Libre de Bruxelles, Brussels, Belgium
[f] Department of Geographical an Earth Sciences, University of Glasgow, Glasgow, Scotland, UK

ARTICLE INFO

Article history:
Received 14 September 2009
Received in revised form 28 December 2009
Accepted 2 January 2010
Available online 11 January 2010

Keywords:
Sea urchin
Spine
Anisotropy
Single crystal
Magnesium
Mechanical properties

ABSTRACT

Sea urchins have characteristic spines that fulfil critical functions. Several studies revealed marked spine internal heterogeneities at different structural levels despite the single-crystal character of the spines. Most of these studies did not speculate about the functional meaning of these heterogeneities. Spine heterogeneities were investigated in the sea urchin *Paracentrotus lividus* and their possible functional implications discussed. Spines mainly show two morphological parts: the base, made of a meshwork stereom, and the shaft, with longitudinal plain septa and a central core of meshwork stereom. Electron Backscatter Diffraction showed no difference in crystallite orientation between the two structures. Atomic Absorption Spectrometry and Energy dispersive X-ray analysis revealed that Mg was not uniformly distributed in the spine. Mg concentration is higher in the inner part of the septa than in the septum outer part. Furthermore, a cyclic pattern of Mg concentration in septa was observed. This is suggested to be linked to the spine ontogeny. Nano- and microindentation analyses revealed that the septa have higher stiffness and hardness than the meshwork stereom and that septum stiffness and hardness present different trends in longitudinal and transverse section. These mechanical heterogeneities may have an adaptive functional value.

1. Introduction

Minerals produced by living organisms usually have remarkable properties in comparison with their abiotic counterparts (Lowenstein and Weiner, 1989). Structural, chemical, and crystallographical features of these biominerals are now better characterized at the nanoscale level (e.g. Weiner et al., 2000; Cölfen and Mann, 2003; Addadi et al., 2006). In contrast, the functional significance of the organism biomineral characteristics is in most cases poorly understood, especially in invertebrates. This paradox is well illustrated by echinoderms, such as sea urchins, starfish and allies, a taxon in which numerous species play key roles in marine ecosystems (Jangoux and Lawrence, 1982).

Echinoderms elaborate a skeleton made of discrete ossicles located in the dermis. Each ossicle consists of a tridimensional network of mineralized trabeculae, the stereom, which delimits an internal and complementary network filled by connective tissue, the stroma. The stereom consists of magnesium calcium carbonate and of 0.1% (w/w) organic material (the intrastereomic organic matrix, IOM) (Weiner, 1985). Most of the mineral phase is in the form of high-magnesium calcite i.e., a solid solution of $CaCO_3$ and $MgCO_3$ (Chave, 1952), but initial deposits are made of amorphous $CaCO_3$ (Politi et al., 2004). Amorphous $CaCO_3$ is a metastable phase, which transforms under abiotic conditions, in a few minutes, into the stable crystalline phase (Brecevic and Nielsen, 1989). Such transformation into calcite also occurs in the stereom but at a much slower pace (Politi et al., 2004). In the calcite phase of the ossicles, the $MgCO_3$ content ranges from 3.0 to 43.5 mol.% (Schroeder et al., 1969), a concentration that would make inorganic calcite metastable under normal temperature/pressure conditions (Lerman, 1965). This calcite phase shows the X-ray diffraction patterns of a single crystal, but also shows conchoidal fractures instead of the expected rhombohedral cleavage of calcite (Donnay and Pawson, 1969). This has been attributed to the inhibition of rhombohedral cleavage planes by the IOM (Berman et al., 1988).

Sea urchins have characteristic spines which play key functional roles. They protect the body from predators and waterbourne particles, are involved in locomotion (acting as stilts in some taxa) and in burrowing (in the so-called "irregular sea urchins"). Each fully grown spine is a single crystal of magnesium calcite, with the *c*-axis oriented along the morphological long axis (Donnay and

* Corresponding author. Address: Laboratoire de Biologie Marine CP 160/15, Université Libre de Bruxelles, Avenue F.D. Roosevelt 50, 1050 Bruxelles, Belgium. Fax: +32 2 6502796.
E-mail address: Claire.Moureaux@ulb.ac.be (C. Moureaux).

1047-8477/$ - see front matter © 2010 Elsevier Inc. All rights reserved.
doi:10.1016/j.jsb.2010.01.003

Pawson, 1969; Berman et al., 1990). It is subdivided into three morphologically distinct parts: a base, a circumferential "bourrelet" (the milled ring), and a shaft. The base is articulated on a tubercle of the test and forms with it a ball-and-socket joint. The base core is made of meshwork stereom. On the contrary, the shaft is usually made of radially arranged septa of compact imperforate stereom that are joined by transverse bridges, leaving deep grooves between the septa. The centre of the spine is, according to the species, either hollow or filled with classical meshwork stereom (Dubois and Ameye, 2001). The plain septa are the spine pillars and present a broad outer part, ideal to meet bending moments from all directions. The central stereom allows the spine to be a lightweight construction and prevents septa from entering the spine centre and breaking the whole spine. The transverse bridges prevent the spine from directly buckling under bending forces (Burkhardt et al., 1983). The proportion between the central stereom and the septa gradually increases toward the tip. Associated with the fact that the spines preferentially break near the spine base, this suggests that the spine skeleton corresponds to the engineering principle of constant strain (Burkhardt et al., 1983).

In most species, spines are numerous and easily handled. This prompted numerous studies on their structure, crystalline properties and composition. Several of these studies revealed marked internal heterogeneities despite the single-crystal character of the spines. Magnesium concentration was reported to differ between the base and the shaft although this was not statistically established (Richter, 1984; Magdans and Gies, 2004). Crystal texture appeared anisotropic in fully grown spines with completed septa, the coherence length being longer along the *c*-axis than in the plane perpendicular to this (Aizenberg et al., 1997). Interestingly, younger spines, without developed septa, did not show significant differences in coherence length as a function of orientation. The volume of the crystal domains in these spines was also smaller than in the fully grown spines. The IOM concentration was reported to be higher in the meshwork stereom than in the septa (Aizenberg et al., 1997). Saccharide composition of the intrastereomic matrix also differs between septa and meshwork stereom (Ameye et al., 2001). Finally, differences in the calcite molecular structure of different parts of the spine were reported by Borzęcka-Prokop et al. (2007). Most of these studies did not speculate about the origin and the functional meaning of these internal heterogeneities. Indeed, such heterogeneities have been demonstrated to modulate functional and particularly mechanical properties in many other skeletal structures like molluscs shells, vertebrates bones and teeth including sea urchin ones (Meyers et al., 2008; Wang and Addadi, 1997). In particular, possible variations of mechanical properties at the nano and microscale were never investigated in the sea urchin spine. The aims of the present work are to further investigate the internal spine heterogeneities including mechanical properties, to establish possible relationships between them in a design perspective, and to address their possible functional implications.

2. Materials and methods

2.1. Collection and preparation of spines

Living specimens of *Paracentrotus lividus* were collected on a rocky shore in the Plougastel–Daoulas peninsula, Brittany, France, in March and October of 2006. Eighteen individuals with mean ± SD tests diameters and heights of 5.06 ± 0.84 cm and 2.65 ± 0.54 cm, respectively, were used. Ambital primary spines with no trace of regeneration were severed from the test of living animals from the first sampling with a microblade. They were cleaned from their associated soft tissues in 3% sodium hypochlorite (20–40 min.), rinsed three times in MilliQ (Millipore) water and air-dried (sodium hypochlorite bleaching does not significantly affect spine mechanical properties (Schinner, 1995). These spines (9.9 ± 2.3 mm in length) were used for mechanical measurements, Electron Backscatter Diffraction (EBSD) and Energy dispersive X-ray analysis (EDX). Specimens from the second sampling were directly frozen after being collected. After thawing, ambital primary spines with no trace of regeneration were severed from the test with a microblade, and cleaned from their associated soft tissues in 2 M NaOH (for analysis) (20–40 min), rinsed three times in MilliQ (Millipore) water and air-dried under a vacuum hood. These spines were used for Atomic Absorption Spectrometry.

2.2. Crystallographic and chemical parameters

2.2.1. Electron Backscatter Diffraction (EBSD)

Four spines were used for EBSD analyses. They were embedded in araldite epoxy resin. Two of them were cut longitudinally at the inner septa level and three transverse sections along the shaft length were performed in the other two spines (just above the milled ring, at mid-shaft and at the end of the shaft). Samples were polished through a series of grinding and polishing steps and finally carbon coated following a pre-established procedure (Cusack et al., 2008). EBSD data were obtained using a field-emission SEM (Quanta FEI 200F) equipped with a TSL EBSD system running OIM version 4 to analyze the data. The SEM was operated in high vacuum mode at 20 kV with spot size 4 and aperture size 4. Final EBSD data sets were partitioned to remove all grains that had a confidence index less than 0.1 using OIM software from EDAX. EBSD data are represented by colour coded crystallographic maps, representing crystallographic planes perpendicular to the investigated section.

2.2.2. Magnesium chemical analysis

2.2.2.1. Atomic absorption spectrometry. Nine spines from each of seven sea urchins were used. Each spine was cross sectioned into four parts: the base and the milled ring, the first 3/12 of the shaft (p1), the next 4/12 of the shaft (p2) and the last 5/12 of the shaft (p3). Three homologous parts of three spines from the same individual were pooled to reach detection limits. Thus, three pools of each spine part were made for each sea urchin. Each pool was weighted and mineralised by the high-pressure microwave method using a Milestone 1200 mega microwave oven (for details see Coteur et al., 2003). The samples were then filtered on glass microfiber filters (1.6 mm mesh size, Whatman International, Maidstone, UK) and Milli-Q water (Millipore, Brussels, Belgium) was added to obtain a final volume of 25 ml. The Mg absorbance, with background correction, was measured using a GBC 906AA spectrometer. The calibration curve was established using Mg standard solutions (certifier, Merck). The accuracy was checked using the CCH-1 certified reference material (Govindaraju, 1994) (for details, see Coteur et al., 2003). Magnesium concentrations in the different parts were compared using a partly nested randomized block design, equivalent to a model III analysis of variance for repeated measures (Dagnelie, 1975; Zar, 1996). « Pools » (random factor) were nested in the random factor « sea urchin » and used as blocking factor. « Part » was the fixed effect factor of interest. Multiple comparisons were carried out using a Model III Tukey's test.

2.2.2.2. Energy dispersive X-ray analysis (EDX). Energy dispersive X-ray analysis was carried out on the same spines block used for the microindentation tests (see Section 2.3.2).The section was polished by abrasion on diamond disks and finally mirror polished with a non-aqueous 1 μm diamond suspension (ESCIL, PS-1MIC). The polished slice was carbon-coated in a Balzers BAF-400 rotary evaporator. The elemental energy X-ray analysis was performed in an environmental SEM (FEI XL30 ESEM-FEG), operating at 10 kV and at a working distance of 10 mm. Nine regions of the spines were

considered by point elemental analysis: three successive regions of a septum, three successive regions of concomitant transverse bridges and three successive regions of central stereom. The analyses were repeated three times for each region on each spine. Analyses were carried out on the surface of 1–10 μm^2 size mineral zones, with a normalized acquisition time of 100 s. The elemental quantitative analysis used an automatic background subtraction and a ZAF correction matrix has been used to calculate the elemental composition in atomic percent. The composition was corrected by subtraction of the coated carbon added for the analyses. The $MgCO_3$ molecular percentage was calculated from the elemental composition in atomic percent. The $MgCO_3$ percentage was compared between the spines and the spine regions by an ANOVA Model III (spine and region as, respectively, random and fixed factors). Multiple comparisons were carried out using a Model III Tukey's test. Two systematic maps were generated on each transverse cut with different resolution parameters, but at the same scale (magnification 150×). The first map obtained a matrix of 512 × 400 pixels (1.667 μm/pixel xy, brightness data range 0–4), and the second one a matrix of 2048 × 1600 pixels (0.417 μm/pixel xy, brightness data range 0–21).

2.3. Mechanical parameters

2.3.1. Nanoindentation tests

Two spines were used for nanoindentation analyses. They were respectively cut transversally just above the milled ring and longitudinally close to the spine axis. The sections were partially embedded in araldite resin leaving the top cut surface free of any resin. Subsequently, the surface was ultra-polished initially with 6 and 3 μm thick diamond paste and finally polished using aluminium oxide (1 and 0.3 μm) and colloidal silica (0.06 μm) to avoid subsurface deformation. A Nanoindenter XP from MTS Systems Corporation was used for analyses. Three series of single indentations applying a maximum load of ±50mN every 50 μm along a line pattern were performed on the transverse section and at milled ring level and mid-shaft positions on the longitudinal section. All testing was programmed in such a way that the loading started when the indenter came into contact with the test surface and the load was maintained for 30 seconds at the pre-specified maximum value before unloading. The sample elastic modulus and hardness value were determined from the unloading curve of indentation test. Multiple loading–unloading cycles were applied at each test point. Data used and presented in this study were based on results from the first indentation cycle since they provide a better assessment of properties for structural features and are less likely to be affected by cracking or subsurface damage. As a preliminary procedure, the load–displacement curves together with optical microscopic images of the indents were examined in order to verify the validity of each indentation measurement. Subsequently, scanning electron micrograph (SEM) images were used to analyse each indentation point in detail to assess if results were affected by cracks, local/surface defects and interfaces of different layers. Indentations affected by such artefacts were excluded for further measurements. A minimum of three valid indentations by spine zone were necessary to calculate the indentation parameters of a zone. Calculation of Young's modulus (E) at maximum load and hardness (H) at maximum load of the test area were performed in each analysis (Pérez-Huerta et al., 2007). E and H were compared between septa and meshwork stereom by a t test in both transverse and longitudinal sections. The nanoindentation results were plotted for representation using the imaging software Surface 7.0.

2.3.2. Microindentation tests

Three spines from one sea urchin were used for microindentation tests. The spines were completely embedded in pre-accelerated polyester (MI 42, Midas Composites) resin, and cut perpendicularly to the spine c-axis at 2 mm above the milled ring. In each spine, the proximal transverse section was used for microindentation tests, the distal one for energy dispersive X-ray analysis (see Section 2.2.2.2). The sections were polished with three successive wet sandpapers (grains 600, 800 and 1200) and with a modular Struers polishing machine with alumina powder. Vickers microhardness of the spines was measured on the polished sections with a Leitz microhardness tester attached to a Leitz metallographic MM5 microscope. Samples were loaded with 5 g (≈50 mN) for 15 s on septa and central stereomic regions and furthermore with 50 g (≈500 mN) for 15 s only on septa regions. For each spine, three successive series of three indentations were made along three septa, distinguishing external, middle and internal parts of the septa, and one series of nine indentations was made in the central stereom. Indentation diagonals were measured from optical micrographs. The Vickers hardness (HV) was calculated from the classical formula $HV = 1.854 \times F/d^2$ (Pa), with F the applied force (N) and d the indentation diagonals mean (m). The results were compared between spines and spine regions using an ANOVA Model III (spine and region as, respectively, random and fixed factors). To approach the fracture toughness values of the different regions of the skeleton, the indentations were qualitatively observed (cracks presence and position) in an environmental SEM (FEI XL30 ESEM-FEG), under the back-scattered electron mode.

2.3.3. Bending tests

Three spines from each of 11 sea urchins were used for bending tests. The spine bases and milled rings were embedded in a pre-accelerated polyester (MI 42, Midas Composites) resin block. This block was fastened in a dedicated home-made holder to generate a cantilevered-beam system, which mimics the natural situation of a spine fixed at its base by its mutable connective tissue. The shafts were tested in flexion until fracture, using an Instron 5543 force testing stand, at a speed of 0.006 cm/min. Deflection and force were recorded at a frequency of 10 Hz. The force was applied at 1/6 of the spine length from the tip of the shaft. The effective lengths tested were measured on enlarged photos by image analysis. When the shaft was not broken level with the resin block, the remaining part of the shafts was severed with a razor blade and measured. The broken shafts were cross-sectioned in four parts of similar length with a razor blade. To examine the distribution of the stereom inside a spine, the correctly oriented portions of the shaft were mounted on an aluminium stub, coated with gold for 5 minutes and observed in a SEM (JEOL JSM-6100). Digital micrographs (resolution: 96 dpi) of the cross sections were recorded. The images were manually thresholded, filtered and imported in image analysis C++ dedicated software which calculates the area and the second moment of area (I_2) of the skeleton cross sections. The apparent Young's modulus (E), characterizing the material stiffness, and the bending strength σB, indicating how much load the material can support before it fractures, were calculated according to linear-elastic beam theory (*leb*) applied to cantilevered-beam system (for details, see Schinner, 1995):

$$E = \frac{stress}{strain} = \frac{F/A}{\Delta L/L}\ (\mathrm{Pa}) \quad ; \quad I_2 = \int Y^2 dA\ (\mathrm{m}^4)$$

$$\downarrow leb$$

$$E = \left(\frac{F_{max}}{\Delta L_e}\right) \times \int_0^L \frac{(x - L_e)^2}{I_2(x)} dx\ (\mathrm{Pa}) \quad ; \quad \sigma B = \frac{F_{max}(L_e - x)d(x)}{2I_2(x)}\ (\mathrm{Pa})$$

with F the force (*max*: at fracture), A the area (in transverse section), ΔL the displacement, L the spine length, (*e*: effective), x spine section position, y distance at the neutral fibre, d diameter of the spine.

The mechanical parameters were compared between the individuals by ANOVA Model II (individual as random factor).

3. Results

3.1. Crystallographic and chemical parameters

3.1.1. Electron Backscatter Diffraction (EBSD)

All the spines diffracted as single calcite crystals with the transverse sections showing the {0 0 0 1} plane of calcite and with the longitudinal sections showing the $\{1\bar{1}100\}$ plane in analyzed samples (Fig. 1). All crystallites were aligned, with an angular dispersion of less than 0.5 degrees, to the *c* and *a* axes in transverse and longitudinal sections, respectively. In the spine central stereom, the transverse bridges and some localized area of the spines base, the diffraction intensity was notably low (Fig. 1).

3.1.2. Magnesium chemical analysis

3.1.2.1. Atomic absorption spectrometry. Magnesium concentrations significantly differed between the base and the shaft ($p_{Tukey} = 0.0002$) but not between the different parts of the shaft ($p_{Tukey} \geqslant 0.12$). The base consistently showed the highest concentration (base: 4.80 ± 0.28 vs p_1: 3.13 ± 0.69, p_2: 2.85 ± 0.28, p_3: 3.03 ± 0.29 – mol.% $MgCO_3$; mean ± SD, $n = 21$, respectively).

3.1.2.2. Energy dispersive X-ray analysis (EDX). Five elements were systematically measured above the detection limit in the spine skeleton: O, C, Ca, Mg and Na (in increasing atomic abundance order). The $MgCO_3$ content is presented, by spine regions, in Fig. 2. The $MgCO_3$ content significantly differed between the spine regions ($p = 0.002$). The maximum Mg concentration was found in the inner part of the septa (5.27 ± 1.07 mol.% $MgCO_3$) and its minimum in the outer part of the septa (2.79 ± 0.27 mol.% $MgCO_3$) (Fig. 2a). The $MgCO_3$ content did not differ between the spines ($p_{=}0.231$). The Mg low resolution mappings showed the Mg content decreases from the inner to the outer part of the septa. The high resolution maps revealed cyclic concentric Mg lines in the septa (Fig. 2b).

3.2. Mechanical parameters

3.2.1. Nanoindentation tests

In the transverse section, stiffness (E) and hardness (H) were significantly higher in the septa than in the central stereom (respectively, $p < 10^{-4}$ and $p = 0.005$) (Table 1 and Fig. 3). In the longitudinal section at milled ring level, E and H were significantly

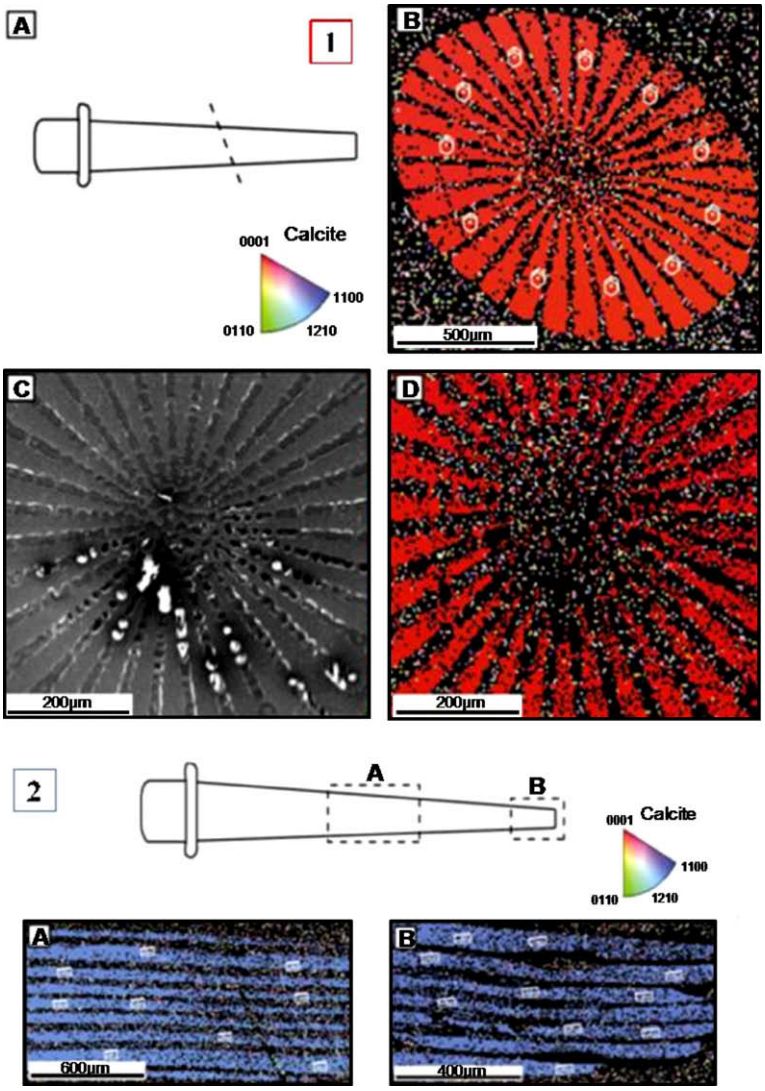

Fig. 1. EBSD analyses of *P. lividus* spine. (1) Transverse and (2) longitudinal cuts. (1A) Cartoon of spine with position of section indicated. Crystallographic orientation map (1B + D) according to colour key in (1A) of region presented in (1C) as the secondary electron image. Wire frames in (1C) indicate that the *c*-axis is parallel with spine length. (2) Cartoon of spine with positions of sections in (2A and B) indicated. (2A and B) are crystallographic orientation maps according to colour key indicating that *c*-axis is parallel with spine length.

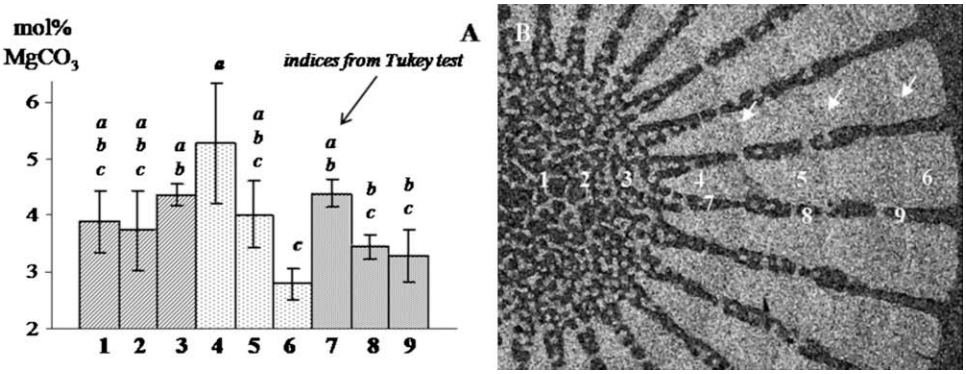

Fig. 2. $MgCO_3$ distribution in transverse sections of *P. lividus* spine. A: Mg concentration in transverse regions measured by EDX analyses (mean ± SD, $n = 3$), 1–3: stereom; 4–6: septa; 7–9: transverse bridges; localization of analyses is indicated in (B). (B) EDX mapping: 0.417 μm/pixel xy, brightness data range: 0–21. arrows = Mg lines.

higher in the septa than in the transverse bridges stereom (respectively, $p = 0.001$, $p < 10^{-4}$) (Table 1). In the mid-shaft longitudinal section, the measurements were just valid for the septa region. The septa E and H of the two longitudinal sections were not different (respectively, $p = 0.6$ and $p = 0.9$). It is noteworthy that, in the septa, *E* was higher in the longitudinal sections and *H* was higher in the transverse section. Both *E* and *H* decreased at the interfaces between skeleton and resin and with imperfections in the polished section by ca. 20% (based on y measurements) (Fig. 3).

3.2.2. Microindentation tests

Hardness measured using 5 and 50 g loads differed, as classically reported (Young and Millman, 1964), and cannot be compared (Table 1). In the tests using 5 g, the central stereom hardness (2.60 ± 0.47 GPa) was significantly lower than the hardness of the septa (average: 4.88 ± 0.12 GPa) ($p < 10^{-4}$). In the tests using 50 g, only carried out on the septa, the hardness of the septa subregions did not differ significantly ($p_{ANOVA} = 0.187$) (average:2.54 ± 0.22 GPa). All indentations were square shaped and fractures occurred for both 5 and 50 g indentations (Fig. 4). They were both star radial and side radial (denominations according to Young and Millman (1964) and only differed by the cracking intensity (notably number of microcracks). Under the same load, the extent of the cracks (determined by apparent cracks length and quantity) differed between the meshwork stereom and the septa and between the inner and the outer part of the septa. The meshwork stereom appeared less resistant to cracking than the septa and the septa inner part less resistant than the outer part.

3.2.3. Bending tests

The force–deflection curves were all linear. The skeleton shaft material was characterized by an apparent Young's modulus of 21.74 ± 3.59 GPa and a bending strength of 108.15 ± 24.82 MPa (mean ± SD). These mechanical parameters were not different between individuals ($p \geqslant 0.23$). The fractures occurred in the proximal part of the shaft, level with the resin block, in 27 of 33 cases. Other fractures randomly occurred within the first 1/2 of the spine length, at min. 15%, max. 44% (min. 1.10 mm–max. 4.56 mm) from the resin block. A spine transverse cut was typically made of a small central mesh stereom and between 28 and 36 septa. The proportion between septa and central stereom generally decreased towards the tip of the shaft. The second moment of area decreased towards the tip of the shaft and was modelled by linear regression. I_2 integrated along the shaft length amounted to 9.75 ± 2.98 × 10^{-16} m^4 and significantly differed between individuals ($p_{ANOVA} = 0.035$).

4. Discussion

4.1. Spine texture

EBSD data are reported for the first time for echinoderms skeleton. Recorded crystallographic orientations correspond to those reported with other techniques for sea urchin spines (for an overview, see (Magdans and Gies, 2004). Meshwork stereom did not diffract well in EBSD, which can be due to a very small size of the crystal domain volume (Griesshaber et al., 2007) and/or to

Table 1
Stiffness (Young's modulus *E*) and hardness (*H*) characterizing locally the *P. lividus* spine skeleton, mean ± SD.

Spine region	Transverse section		Longitudinal section 1 (milled ring level)		Longitudinal section 2 (mid-shaft)	
	E (GPa)	*H* (GPa)	*E* (GPa)	*H* (GPa)	*E* (GPa)	*H* (GPa)
A. Nanoindentation tests (n = 7–11, per spine region)						
Septa	58.57 ± 3.76	3.84 ± 0.25	65.50 ± 5.44	2.71 ± 0.30	64.47 ± 3.01	2.73 ± 0.34
Central stereom	32.20 ± 3.26	1.76 ± 0.70				
Transverse bridges			25.86 ± 9.35	0.69 ± 0.19		
B. Microindentation tests (n = 3, spines)						
Spine region			Weight			
			H_{5g} (GPa)			H_{50g} (GPa)
Septa outer zone			4.76 ± 0.35			2.78 ± 0.13
Septa middle zone			4.99 ± 0.08			2.50 ± 0.19
Septa inner zone			4.88 ± 0.15			2.34 ± 0.08
Central stereom			2.60 ± 0.47			

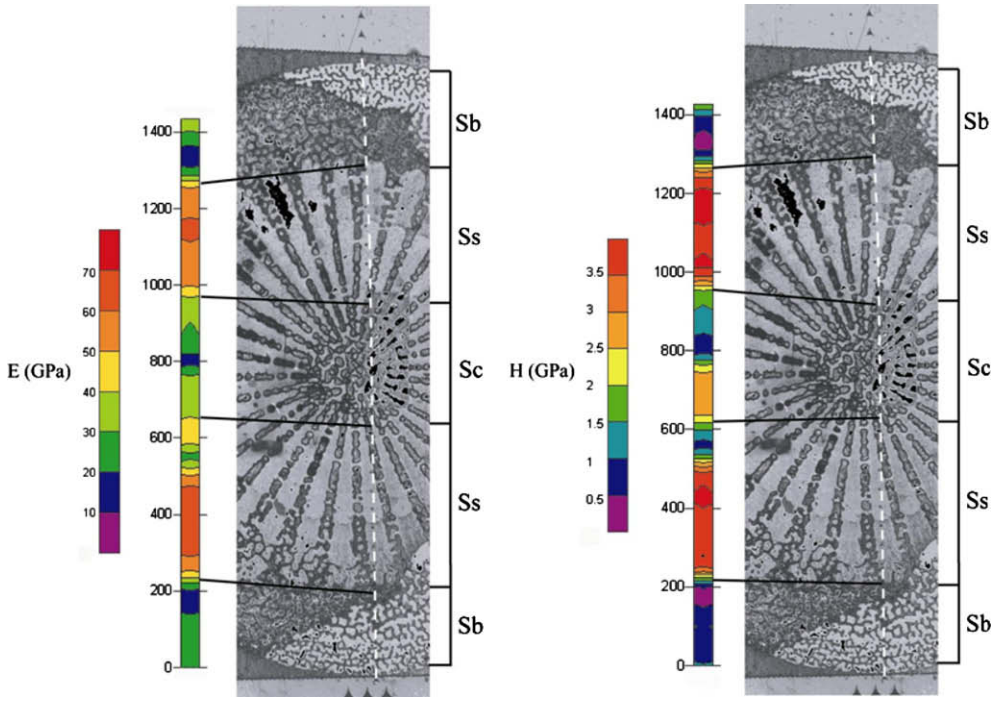

Fig. 3. Maps of stiffness (Young's modulus *E*) and hardness (*H*) of a *P. lividus* spine transverse section (at spine milled ring level) established by nanoindentation. Sb: stereom of the spine base, Ss: septa, Sc: stereom of the spine centre.

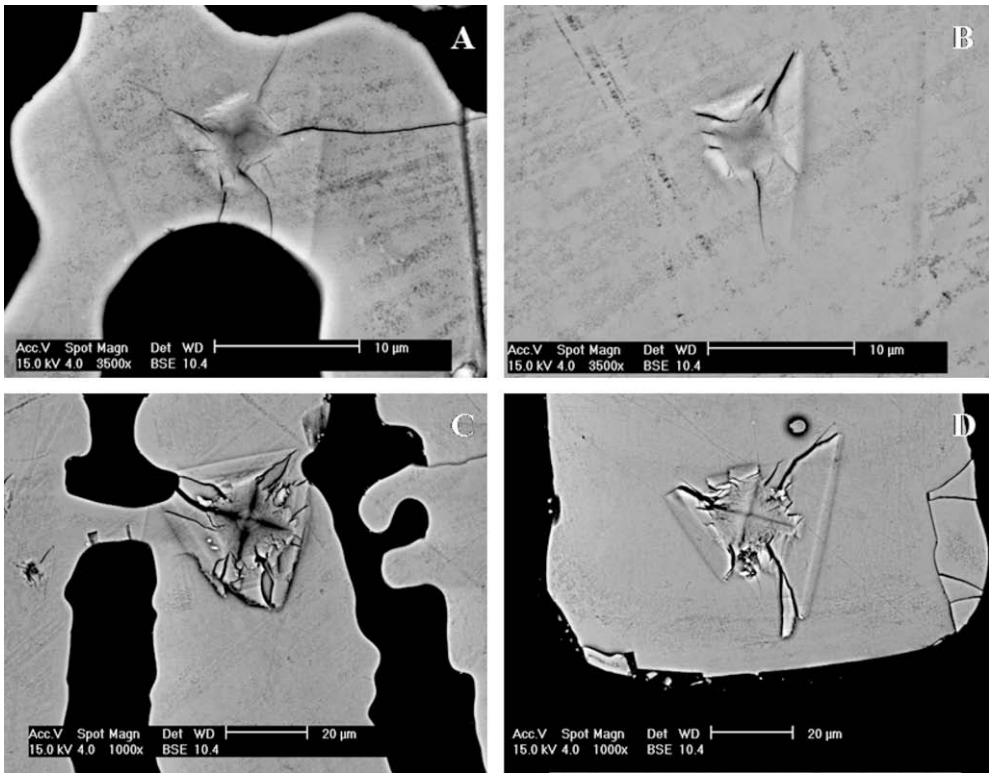

Fig. 4. SEM micrographs of typical microindentation traces in *P. lividus* spine. (A, B) 5 g, A. stereom–B. septa ; (C, D) 50 g, C. inner part–D. outer part.

the presence of a non-crystalline phase, either organic material, amorphous mineral phase or crystalline phase not well-crystallized (Lee and Kim, 2008). The crystal domain volume is actually higher in the stereom than in the septa, but a higher organic matrix concentration was indeed reported in the meshwork (Aizenberg et al., 1997) and could explain the results.

4.2. Magnesium distribution

The atomic absorption spectrometry results statistically confirm that the Mg concentration is higher in the spine base than in the shaft (Magdans and Gies, 2004). EDX data show that the Mg concentration was higher in the inner part of the septa in com-

parison with the septum outer part. The change in Mg concentration within the septa shows a cyclical pattern. We suggest that these differences are related to spine ontogeny. Indeed, during the spine growth, the first deposited skeleton is a meshwork stereom. The septa are formed during a second wave of mineralization during which pores of the skeleton are filled. Further growth of the spine is then occurring by a thickening of the outer part of the septa (for a review, see Dubois and Ameye, 2001). These successive processes are probably linked to the anisotropies reported for the organic matrix concentration and the size of crystal domains (Aizenberg et al., 1997) as well as for Mg concentration (this study). Indeed, the first meshwork stereom is initially deposited as amorphous $CaCO_3$ that subsequently transforms into calcite (Politi et al., 2004). The hydration of this amorphous phase, favoured by acidic organic macromolecules, allows a high incorporation of Mg, which is maintained when the amorphous phase transforms into calcite (Cheng et al., 2007). On the contrary, the pore filling and the septum thickening could proceed through a direct crystallization on the existing template without a transient amorphous phase. In this case, less Mg could be included due to its unfavoured incorporation in the calcite lattice. In the inner part of the septa, the proportion of original stereom is much higher than that of infilling; in contrast, in the outer septum, much more infilling is present. Therefore, more Mg could be included in the inner part. Growth rate has also been suggested to influence Mg incorporation (Weber, 1969). However, recent results indicated that growth rate *per se* does not modify Mg concentration in the echinoderm skeleton (Borremans et al., 2009). Finally, qualitative or quantitative differences in the organic matrix of mineralization secreted during different stages of spine growth could also account for the observed effects. Indeed, Robach et al. (2006) showed that, in a sea urchin tooth, higher Mg concentrations mapped together with matrix molecules richer in aspartic acid, and Stephenson et al. (2008) revealed that, in the presence of a simple hydrophylic peptide with the same carboxyl-rich character as that of matrix typical macromolecules, the Mg incorporation in growing calcite increases significantly. It is noteworthy that Ameye et al. (2001) reported differences in matrix molecules from the septa and the central stereom.

4.3. Stiffness

The stereom and septa showed significantly different stiffness. Now, in the stereom, the interface with the embedding material is much higher than in the septa and this could result in lower E and H values. However, indentation parameters at stereom and septa interfaces showed very different values (Fig. 3). This strongly suggests that the different interface ratios between stereom and septa cannot account for the recorded E and H differences between them. Nanoindentation revealed that stiffness is higher in the septa than in the central stereom and transverse bridges. Furthermore, septum stiffness in longitudinal section was higher than in transverse section. Such differences in material stiffness are usual in complex polycrystalline biominerals as vertebrate long bones (Ziv et al., 1996; Rho. et al., 2001; Fan et al., 2002), but are reported for the first time, to our knowledge, for a biogenic single-crystal. We suggest that local variations in concentration, nature and distribution of the intrastereomic matrix and consequently in crystal texture, produced the observed local mechanical differences. The volumes of crystal domains are smaller in the septa than in the meshwork stereom, which results in a denser material which will have normally higher intrinsic mechanical properties. Furthermore the preferential distribution of the intrastereomic matrix in longitudinal planes would also play a role, because the intrastereomic matrix can be considered as a cohesive material to a certain extent. It could notably explain the anisotropic mechanical comportment of the structure. The apparent Young's modulus measured by the bending test amounted to 22 GPa and was three times lower than that measured in the septa by nanoindentation. The bending test result is, however, mainly determined by the material far from the neutral axis—the axis in the cross section of a beam along which there are no longitudinal stresses or strains (here $\sim$ the geometric centroid)—here the septa. Such a discrepancy, with an underestimation of elastic modulus from bending test, has often been reported for vertebrate bones due to the different techniques used to obtain the results (i.e. Van Lenthe et al., 2008), but is particularly important here. It could be explained by different factors, namely an overestimate of the second moment of area (at meshwork stereom level), differences in sample preparation, and the calculation based on a supposed isotropic material.

4.4. Hardness

Both micro- and nanoindentations showed a significantly higher hardness in the septa than in the central stereom. In microindentation, cracks were longer in the meshwork stereom at variable loads. These results agree with stereom and septa stiffness data and could be explained by the same hypothesis. On the contrary the hardness of the septa appeared higher in transverse sections (i.e. indentation parallel to the c-axis) than in longitudinal section (perpendicular to the c-axis), which is puzzling considering the opposite Young's modulus trend. It is noteworthy that higher indentation parameters in transverse sections compared to longitudinal ones are usually observed in complex polycrystalline structure such as vertebrate long bones (Ziv et al., 1996; Rho et al., 2001; Fan et al., 2002). This difference in E and H values in different planes can be attributed to the very specific intrasteromic matrix distribution in calcite planes. The matrix would be a complex cohesive material which can finely manage the local mechanical properties.

Interestingly, the hardness did not correlate here with Mg concentration contrary to calcite polycrystalline calcite of the sea urchin tooth (Wang and Addadi, 1997) and inorganic calcite with low magnesium substitution (Klein, 2002). That would mean that structural aspects independent from Mg incorporation, such as crystal domain volumes or degree of crystallinity, play the major role in hardness properties.

4.5. Functional aspects

Aizenberg (Aizenberg, 2006) considered the echinoderm skeleton as a fibre-reinforced composite material—with crystal domains as fibres and intrastereomic matrix as reinforcing guest. Fine mechanical modulations appeared to be produced by differences in crystal domain volumes and in organic matrix concentration and distribution (Fig. 5). As a first consequence, septa revealed to be globally harder and stiffer. Actually, septa have to meet the main part of bending moments and abrasion forces to which the spines are submitted. These constraints are essentially generated by hydrodynamic forces resulting in impact and friction against the rocky substrate, by predators trying to reach the test and by impacting particles. On the other hand, mechanical quality of skeleton material near to spine centre is lower. This can also be viewed as an adaptation. The material near beam centre is much less essential for beam mechanical potential, resistance to impact and surface mechanics. So, having a less efficient material at this level is not a problem. On the contrary, a lighter and energetically less expensive material may be a biological advantage. This is further supported by the occurrence in some species of hollow where this material is absent. Furthermore the septa lightly differed in their mechanical properties according to orientation. This anisotropy is puzzling because stiffness and hardness present opposite trends,

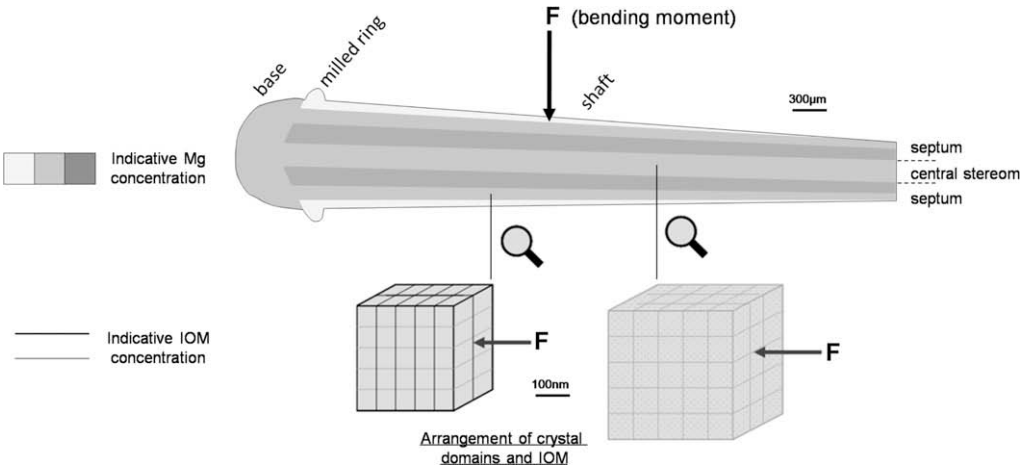

Fig. 5. Schematic illustration of *P. lividus* spine (longitudinal section) showing Mg relative distribution and structural elements which are proposed to be first responsible for shaft specific mechanical behaviour: relative crystal domain volumes and intrastereomic organic matrix (IOM) relative concentration and distribution.

which is very unusual. In particular, the higher Young's modulus apparently does not correspond to stress during spine bending. Studies should be carried further on the detailed functional loading of the spine to approach this question.

Acknowledgments

We thank Jacques Jedwab for fruitful discussions and help micr-oindentation and Philippe Pernet for technical support. Claire Moureaux was holder of a Belgian FRIA grant and Philippe Dubois is a Senior Research Associate of the NFSR (Belgium). The study was supported by FRFC Contract 2.4532.07. Alberto Pérez-Huerta and Maggie Cusack acknowledge financial support from the BBSRC (BB/E003265/1).

References

Addadi, L., Joester, D., Nudelman, F., Weiner, S., 2006. Mollusk shell formation: a source of new concepts for understanding biomineralization processes. Chem. Eur. J. 12, 980–987.

Aizenberg, J., 2006. Nanomechanics of biological single crystals. The role of intracristalline Proteins. In: Chuang, T.J., et al. (Eds.), Nanomechanics of Materials and Structures. Springer, Netherlands, pp. 99-108.

Aizenberg, J., Hanson, J., Koetzle, T.F., Weiner, S., Addadi, L., 1997. Control of Macromolecule Distribution within Synthetic and Biogenic Single Calcite Crystals. J. Am. Chem. Soc. 119, 881–886.

Ameye, L., De Becker, G., Killian, C., Wilt, F., Kemps, R., Kuypers, S., Dubois, P., 2001. Proteins and saccharides of the sea urchin organic matrix of mineralization: characterization and localization in the spine skeleton. J. Struct. Biol. 134, 56–66.

Berman, A., Addadi, L., Weiner, S., 1988. Interaction of sea urchin skeleton macromolecules with growing calcite crystals—a study of intracristalline composite material. Nat. Lond. 331, 546–548.

Berman, A., Addadi, L., Kvick, A., Leiserowitz, L., Nelson, M., Weiner, S., 1990. Intercalation of Sea Urchin Proteins in Calcite: Study of a Crystalline Composite Material. Science 250, 664–667.

Borremans, C., Hermans, J., Baillon, S., André, L., Dubois, P., 2009. Salinity effects on the Mg/Ca and Sr/Ca in starfish skeletons and the echinoderm relevance for paleoenvironmental reconstructions. Geology 37 (4), 351–354.

Borzęcka-Prokop, B., Wesełucha-Birczyńska, A., Koszowska, E., 2007. MicroRaman, PXRD, EDS and microscopic investigation of magnesium calcite biomineral phases. The case of sea urchin biominerals. J. Mol. Struct. 828, 80–90.

Brecevic, L., Nielsen, A.E., 1989. Solubility of amorphous calcium carbonate. J. Cryst. Growth 98, 504–510.

Burkhardt, A., Hansmann, W., Märkel, K., Niemann, H., 1983. Mechanical Design in Spines of Diadematoid Echinoids (Echinodermata, Echinoidea). Zoomorphology 102, 189–203.

Chave, K.E., 1952. A solid solution between calcite and dolomite. J. Geol. 60, 190–192.

Cheng, X., Varona, P.L., Olszta, M.J., Gower, L.B., 2007. Biomimetic synthesis of calcite films by a polymer-induced liquid-precursor (PILP) process 1. Influence and incorporation of magnesium. J. Cryst. Growth 307, 395–404.

Cölfen, H., Mann, S., 2003. Higher-order organization by mesoscale self-assembly and transformation of hybrid nanostructures. Angew. Chem. Int. 42, 2350–2365.

Coteur, G., Pernet, P., Gillan, D., Joly, G., Maage, A., Dubois, P., 2003. Field contamination of the starfish *Asterias rubens* by metal. Part 1: short- and long-term accumulation along a pollution gradient. ETC 9, 2136–2144.

Cusack, M., England, J., Parkinson, D., Dalbeck, P., Lee, M.R., Curry, G.B., Fallick, A.E., 2008. Oxygen isotope composition, magnesium distribution and crystallography of *Terebratulina retusa*. Fossils Strata 54, 259–269.

Dagnelie, P., 1975. Théorie et Méthodes Statistiques, vol. 2. Les presses agronomiques de Gembloux, Gembloux.

Donnay, G., Pawson, D.L., 1969. X-ray diffraction studies of echinoderm plates. Science 166, 1147–1150.

Dubois, P., Ameye, L., 2001. Regeneration of spines and pedicellariae in echinoderms: a review. Microsc. Res. Tech. 55, 427–437.

Fan, Z., Swedener, J.G., Rho, J.-Y., Roy, M.E., Pharr, G.M., 2002. Anisotropic properties of human tibial cortical bone as measured by nanoindentation. J. Orthop. Res. 20, 806–810.

Govindaraju, K., 1994. Compilation of working values and sample description for 383 geostandards. Geostand. Newslett. 18, 1.

Griesshaber, E., Schmahl, W.W., Neuser, R., Pettke, T., Blüm, M., Mutterlose, J., Brand, U., 2007. Crystallographic texture and microstructure of terebratulide brachiopod shell calcite: an optimized materials design with hierarchical architecture. Am. Miner. 92 (5–6), 722–734.

Jangoux, M., Lawrence, J.M., 1982. Echinoderm Nutrition. Balkema, Rotterdam.

Klein, C., 2002. Mineral Science, 22nd ed. John Wiley & Sons, Inc., New York.

Lee, S.W., Kim, G.H., Choi, C.S., 2008. Characteristics crystal orientation of folia in oyster shell, *Crassostrea gigas*. MSE C28, 258–263.

Lerman, A., 1965. Strontium and magnesium in water and in *Crassostrea* calcite. Science 150, 745–751.

Lowenstein, H.A., Weiner, S., 1989. On Biomineralization. Oxford University Press, New York.

Magdans, U., Gies, H., 2004. Single crystal structure analysis of sea urchin spine calcites: systematic investigations of the Ca/Mg distribution as a function of habitat of the sea urchin and the sample location in the spine. Eur. J. Mineral. 16, 261–268.

Meyers, M.A., Chen, P.-Y., Lin, A.Y.-M., Seki, Y., 2008. Biological materials: structure and mechanical properties. Prog. Mat. Sci. 53, 1–206.

Pérez-Huerta, A., Cusack, M., Zhu, W., England, J., Hughes, J., 2007. Material properties of brachiopod shell ultrastructure by nanoindentation. J. R. Soc. Interface 4 (12), 33–39.

Politi, Y., Arad, T., Klein, E., Weiner, S., Addadi, L., 2004. Sea urchin spine calcite forms via a transient amorphous calcium carbonate phase. Science 306, 1161–1164.

Rho, J.-Y., Currey, J.D., Zioupos, P., Pharr, G.M., 2001. The anisotropic Young's modulus of equine secondary osteones and interstitial bone determined by nanoindentation. J. Exp. Biol. 204, 1775–1781.

Richter, D.K., 1984. Zur zusammensetzung und diagenese natürlicher Mg–calcite. Bochumer geologische und geotechnische Arbeiten 15.

Robach, J.S., Stock, S.R., Veis, A., 2006. Mapping of magnesium and of different protein fragments in sea urchin teeth via secondary ion mass spectroscopy. J. Struct. Biol 155, 87–95.

Schinner, G.O., Peterlik, Hilgers, H., Kromp, K., 1995. Structural design of mechanical properties in spines of Spatangoid sea urchins. Biomimetics 3, 13–30.

Schroeder, J.H., Dwornik, E.J., Papike, J.J., 1969. Primary protodolomite in echinoïd skeleton. Geol. Soc. Am. Bull. 80, 1613–1616.

Stephenson, A.E., deYoreo, J.J., Wu, L., Wu, K.J., Hoyer, J., Dove, P.M., 2008. Peptides enhance magnesium signature in calcite: insights into origins of vital effects. Science 322, 724–727.

Van Lenthe, G.H., Voide, R., Boyd, S.K., Müller, R., 2008. Tissue modulus calculated from beam theory is biased by bone size and geometry: implications for the use of three-point bending tests to determine bone tissue modulus. Bone 43, 717–723.

Wang, R.Z., Addadi, L., Weiner, S., 1997. Design strategies of sea urchin teeth: structure, composition and micromechanical relations to function. Phil. Trans. R. Soc. Lond. B 352, 469–480.

Weber, J.N., 1969. The incorporation of magnesium into the skeletal calcites of echinoderms. Am. J. Sci. 267, 537–566.

Weiner, S., 1985. Organic matrix-like macromolecules associated with the mineral phase of sea urchin skeletal plates and teeth. J. Exp. Zool. 234, 7–15.

Weiner, S., Addadi, L., Wagner, H.D., 2000. Material design in biology. Mater. Sci. Eng. C 11, 1–8.

Young, B.B., Millman, A.P., 1964. Microhardness and deformation characteristics of ore minerals. Trans. Inst. Mining Metall. 73, 437–466.

Zar, J.H., 1996. Biostatistical Analysis, fourth ed. Prentice-Hall Int. Ltd., London.

Ziv, V., Wagner, H.D., Weiner, S., 1996. Microstructure–microhardness relations in parallel-fibered and lamellar bone. Bone 18 (5), 417–428.